Measurement of *CP* Asymmetries in $B^0 \to K^0_S \pi^0 \gamma$ Decays at Belle II

I. Adachi, L. Aggarwal, H. Ahmed, H. Aihara, N. Akopov, A. Aloisio, N. Anh Ky, D. M. Asner, H. Atmacan, T. Aushev, V. Aushev, M. Aversano, R. Ayad, V. Babu, H. Bae, S. Bahinipati, P. Bambade, Sw. Banerjee, S. Bansal, M. Barrett, J. Baudot, A. Baur, A. Beaubien, F. Becherer, J. Becker, J. V. Bennett, F. U. Bernlochner, V. Bertacchi, M. Bertemes, E. Bertholet, M. Bessner, S. Bettarini, B. Bhuyan, F. Bianchi, L. Bierwirth, T. Bilka, S. Bilokin, D. Biswas, D. Bodrov, A. Bolz, A. Bondar, J. Borah, A. Boschetti, A. Bozek, M. Bračko, P. Branchini, R. A. Briere, T. E. Browder, A. Budano, S. Bussino, M. Campajola, L. Cao, G. Casarosa, C. Cecchi, J. Cerasoli, M.-C. Chang, P. Chang, R. Cheaib, P. Cheema, C. Chen, B. G. Cheon, K. Chilikin, K. Chirapatpimol, H.-E. Cho, K. Cho, S.-J. Cho, S.-K. Choi, S. Choudhury, J. Cochran, L. Corona, J. X. Cui, S. Das, F. Dattola, E. De La Cruz-Burelo, S. A. De La Motte, G. De Nardo, M. De Nuccio, G. De Pietro, R. de Sangro, M. Destefanis, S. Dey, R. Dhamija, A. Di Canto, F. Di Capua, J. Dingfelder, Z. Doležal, I. Domínguez Jiménez, T. V. Dong, M. Dorigo, D. Dorner, K. Dort, D. Dossett, S. Dreyer, S. Dubey, K. Dugic, G. Dujany, P. Ecker, M. Eliachevitch, P. Feichtinger, T. Ferber, D. Ferlewicz, T. Fillinger, C. Finck, G. Finocchiaro, A. Fodor, F. Forti, A. Frey, B. G. Fulsom, A. Gabrielli, E. Ganiev, M. Garcia-Hernandez, R. Garg, G. Gaudino, V. Gaur, A. Gaz, A. Gellrich, G. Ghevondyan, D. Ghosh, H. Ghumaryan, G. Giakoustidis, R. Giordano, A. Giri, A. Glazov, B. Gobbo, R. Godang, O. Gogota, P. Goldenzweig, W. Gradl, T. Grammatico, E. Graziani, D. Greenwald, Z. Gruberová, T. Gu, Y. Guan, K. Gudkova, S. Halder, Y. Han, K. Hara, T. Hara, K. Hayasaka, H. Hayashii, S. Hazra, C. Hearty, M. T. Hedges, A. Heidelbach, I. Heredia de la Cruz, M. Hernández Villanueva, T. Higuchi, M. Hoek, M. Hohmann, P. Horak, C.-L. Hsu, T. Humair, T. Iijima, K. Inami, N. Ipsita, A. Ishikawa, R. Itoh, M. Iwasaki, P. Jackson, W. W. Jacobs, D. E. Jaffe, E.-J. Jang, Q. P. Ji, S. Jia, Y. Jin, K. K. Joo, H. Junkerkalefeld, M. Kaleta, D. Kalita, A. B. Kaliyar, J. Kandra, K. H. Kang, S. Kang, G. Karyan, T. Kawasaki, F. Keil, C. Kiesling, C.-H. Kim, D. Y. Kim, K.-H. Kim, Y.-K. Kim, H. Kindo, K. Kinoshita, P. Kodyš, T. Koga, S. Kohani, K. Kojima, A. Korobov, S. Korpar, E. Kovalenko, R. Kowalewski, T. M. G. Kraetzschmar, P. Križan, P. Krokovny, T. Kuhr, Y. Kulii, J. Kumar, M. Kumar, K. Kumara, T. Kunigo, A. Kuzmin, Y.-J. Kwon, S. Lacaprara, Y.-T. Lai, T. Lam, L. Lanceri, J. S. Lange, M. Laurenza, R. Leboucher, F. R. Le Diberder, M. J. Lee, P. Leo, D. Levit, C. Li, L. K. Li, S. X. Li, Y. Li, Y. B. Li, J. Libby, Y.-R. Lin, M. H. Liu, Q. Y. Liu, Z. Q. Liu, D. Liventsev, S. Longo, T. Lueck, T. Luo, C. Lyu, Y. Ma, M. Maggiora, S. P. Maharana, R. Maiti, S. Maity, G. Mancinelli, R. Manfredi, E. Manoni, M. Mantovano, D. Marcantonio, S. Marcello, C. Marinas, L. Martel, C. Martellini, A. Martini, T. Martinov, L. Massaccesi, M. Masuda, K. Matsuoka, D. Matvienko, S. K. Maurya, J. A. McKenna, R. Mehta, F. Meier, M. Merola, F. Metzner, C. Miller, M. Mirra, S. Mitra, K. Miyabayashi, H. Miyake, R. Mizuk, G. B. Mohanty, N. Molina-Gonzalez, S. Mondal, S. Moneta, H.-G. Moser, M. Mrvar, R. Mussa, I. Nakamura, K. R. Nakamura, M. Nakao, H. Nakazawa, Y. Nakazawa, A. Narimani Charan, M. Naruki, D. Narwal, Z. Natkaniec, A. Natochii, L. Nayak, M. Nayak, G. Nazaryan, M. Neu, C. Niebuhr, S. Nishida, S. Ogawa, Y. Onishchuk, H. Ono, Y. Onuki, P. Oskin, F. Otani, P. Pakhlov, G. Pakhlova, A. Panta, S. Pardi, K. Parham, H. Park, S.-H. Park, B. Paschen, A. Passeri, S. Patra, S. Paul, T. K. Pedlar, R. Peschke, R. Pestotnik, M. Piccolo, L. E. Piilonen, G. Pinna Angioni, P. L. M. Podesta-Lerma, T. Podobnik, S. Pokharel, C. Praz, S. Prell, E. Prencipe, M. T. Prim, I. Prudiiev, H. Purwar, P. Rados, G. Raeuber, S. Raiz, N. Rauls, K. Ravindran, M. Reif, S. Reiter, M. Remnev, I. Ripp-Baudot, G. Rizzo, S. H. Robertson, M. Roehrken, J. M. Roney, A. Rostomyan, N. Rout, G. Russo, D. A. Sanders, S. Sandilya, A. Sangal, L. Santelj, Y. Sato, V. Savinov, B. Scavino, C. Schmitt, C. Schwanda, A. J. Schwartz, M. Schwickardi, Y. Seino, A. Selce, K. Senyo, J. Serrano, M. E. Sevior, C. Sfienti, W. Shan, X. D. Shi, T. Shillington, T. Shimasaki, J.-G. Shiu, D. Shtol, B. Shwartz, A. Sibidanov, F. Simon, J. B. Singh, J. Skorupa, R. J. Sobie, M. Sobotzik, A. Soffer, A. Sokolov, E. Solovieva, S. Spataro, B. Spruck, M. Starič, P. Stavroulakis, S. Stefkova, R. Stroili, M. Sumihama, K. Sumisawa, W. Sutcliffe, H. Svidras, M. Takahashi, M. Takizawa, U. Tamponi, S. Tanaka, K. Tanida, F. Tenchini, A. Thaller, O. Tittel, R. Tiwary, D. Tonelli, E. Torassa, K. Trabelsi, I. Tsaklidis, M. Uchida, I. Ueda, Y. Uematsu, T. Uglov, K. Unger, Y. Unno, K. Uno, S. Uno, P. Urquijo, Y. Ushiroda, S. E. Vahsen, R. van Tonder, K. E. Varvell, M. Veronesi,

A. Vinokurova, V. S. Vismaya, L. Vitale, V. Vobbilisetti, R. Volpe, B. Wach, M. Wakai, S. Wallner, E. Wang, M.-Z. Wang, X. L. Wang, Z. Wang, A. Warburton, M. Watanabe, S. Watanuki, C. Wessel, E. Won, Y. Xie, X. P. Xu, B. D. Yabsley, S. Yamada, S. B. Yang, J. Yelton, J. H. Yin, K. Yoshihara, C. Z. Yuan, Y. Yusa, L. Zani, F. Zeng, B. Zhang, Y. Zhang, V. Zhilich, Q. D. Zhou, X. Y. Zhou, V. I. Zhukova, and R. Žlebčík

(Belle II Collaboration)

(Received 20 July 2024; accepted 28 October 2024; published 2 January 2025)

We report measurements of time-dependent CP asymmetries in $B^0 \to K^0_S\pi^0\gamma$ decays based on a data sample of $(388 \pm 6) \times 10^6$ $B\bar{B}$ events collected at the $\Upsilon(4S)$ resonance with the Belle II detector. The Belle II experiment operates at the SuperKEKB asymmetric-energy e^+e^- collider. We measure decay-time distributions to determine CP -violating parameters S and C. We determine these parameters for two ranges of $K^0_S\pi^0$ invariant mass: $m(K^0_S\pi^0) \in (0.8, 1.0)$ GeV/c^2, which is dominated by $B^0 \to K^{*0}(\to K^0_S\pi^0)\gamma$ decays, and a complementary region $m(K^0_S\pi^0) \in (0.6, 0.8) \cup (1.0, 1.8)$ GeV/c^2. Our results have improved precision as compared to previous measurements and are consistent with theory predictions.

DOI: 10.1103/PhysRevLett.134.011802

Flavor-changing neutral current decays of elementary particles are of great interest since they predominantly occur through quantum loop-level processes, making them highly sensitive to phenomena beyond the standard model (SM). Because of the heavy b quark mass and enhanced loop contribution of the t quark, processes involving the $b \to s$ quark transition are especially sensitive to physics beyond the SM (BSM). Decays via the $b \to s\gamma$ radiative transition are similarly important and have thus been studied both theoretically and experimentally [1–3]. In particular, the polarization of the final-state photon adds unique sensitivity to BSM physics [4–11]. In the SM, because W bosons interact only with left-handed fermions, the s quark from $b \to s\gamma$ (a $\bar{B}^0$ decay) is left-handed and thus the outgoing photon must have negative helicity to conserve angular momentum along the decay axis. Similarly, the outgoing photon from a B^0 decay must have positive helicity. The "wrong" photon polarization is possible only if the s quark flips its chirality, which suppresses this process by a factor of m_s/m_b.

In coherent B-pair production via $e^+e^- \to \Upsilon(4S) \to B^0\bar{B}^0$, the time-dependent decay rate of one B meson, denoted $B_{\rm sig}$, decaying into $K^0_S(\to \pi^+\pi^-)\pi^0 \times (\to \gamma\gamma)\gamma$, and the accompanying B meson, denoted $B_{\rm tag}$, decaying with flavor q ($q = 1$ for $B^0_{\rm tag}$ and -1 for $\bar{B}^0_{\rm tag}$), is given by [12–15]

$$\mathcal{P}(\Delta t, q) = \frac{e^{-|\Delta t|/\tau_{B^0}}}{4\tau_{B^0}}\{1 + q[S\sin(\Delta m_d \Delta t) - C\cos(\Delta m_d \Delta t)]\}, \quad (1)$$

where $\Delta t \equiv t_{\rm sig} - t_{\rm tag}$ is the difference between the proper decay times of $B_{\rm sig}$ and $B_{\rm tag}$, S and C are parameters characterizing mixing-induced and direct CP violation [16], respectively, τ_{B^0} is the B^0 lifetime, and Δm_d is the mass difference between the two neutral B-meson mass eigenstates. In the SM, the S value is expected to be very small, as the different photon polarizations distinguish between otherwise identical final states originating from B^0 or $\bar{B}^0$ and thus preclude interference [4,5]. However, if right-handed currents from BSM physics contribute, a B^0 ($\bar{B}^0$) could more easily emit negative (positive) helicity photons, leading to sizable interference and $S \sim \mathcal{O}(0.1)$ [6–11]. For resonant $B^0 \to K^*(892)^0(\to K^0_S\pi^0)\gamma$ [17], two SM calculations give $S = (-3.5 \pm 1.7) \times 10^{-2}$ [18] and $(-2.3 \pm 1.6) \times 10^{-2}$ [19]. Nonresonant $B^0 \to K^0_S\pi^0\gamma$ decays could include a long-distance contribution from $b \to (c\bar{c})s$ rescattering and should be measured separately [20,21]. The C value in these decays has not been reliably estimated [16].

Previously, the Belle and *BABAR* experiments measured the S values in $B^0 \to K^0_S\pi^0\gamma$ decays with a precision of about 30% [22,23]. The LHCb experiment also measured the photon polarization in $b \to s\gamma$ transitions [24–26]. In addition, these experiments measured the direct CP asymmetry with 2% precision [27–29]. These results are consistent with SM predictions, although BSM contributions cannot be excluded. In this Letter, we report new measurements of time-dependent CP asymmetries in $B^0 \to K^*(892)^0\gamma$ and nonresonant $B^0 \to K^0_S\pi^0\gamma$ decays using

365 fb^{-1} of data [30], corresponding to $(388 \pm 6) \times 10^6$ $B\bar{B}$ events, recorded by the Belle II experiment from 2019 to 2022 [31].

Belle II [31] operates at the SuperKEKB collider [32], which collides 7.0 GeV electrons with 4.0 GeV positrons. The detector components most relevant for this measurement are a two-layer silicon-pixel detector (PXD), a four-layer double-sided silicon-strip detector (SVD) [33], and a 56-layer central drift chamber (CDC). These detectors reconstruct tracks of charged particles and measure displaced vertices. Only one-sixth of the second PXD layer was installed for the data analyzed here. The symmetry axis of these cylindrical detectors, defined as the z axis, is almost collinear with the electron beam direction. The detector coverage is divided into three regions depending on the polar angle θ: the barrel for $32.2° < \theta < 128.7°$, and the forward and backward end caps for $12.4° < \theta < 31.4°$ and $130.7° < \theta < 155.1°$, respectively. Surrounding the CDC is a time-of-propagation counter [34] in the barrel and an aerogel-based ring-imaging Cherenkov counter in the forward end cap. These detectors provide charged-particle identification (PID). Surrounding the PID detectors is an electromagnetic calorimeter (ECL) based on CsI(Tl) crystals that provides energy and timing measurements for photons and electrons. The subdetectors described above are enclosed within a superconducting solenoid that provides a 1.5 T magnetic field oriented in the z direction.

We use Monte Carlo simulation to optimize event selection criteria, calculate reconstruction efficiencies, and study sources of background. We generate simulated signal samples of $B^0 \to K^*(892)^0\gamma$, $B^0 \to K_2^{*0}(1430)\gamma$, $B^0 \to K^{*0}(1680)\gamma$, and nonresonant $B^0 \to K_S^0\pi^0\gamma$ [35]. To model backgrounds, we generate samples of $e^+e^- \to B^0\bar{B}^0$, B^+B^-, $q\bar{q}$ ($q = u, d, s, c$), and $\tau^+\tau^-$. We use EvtGen [36] for hadronic decays, KKMC [37] followed by fragmentation by Pythia [38] for $q\bar{q}$, and Tauola [39] for τ decays. The detector response is simulated with Geant4 [40]. We analyze data and simulated events using the Belle II software [41]. We optimize [42] selection criteria for mass windows, momentum, and boosted decision trees (BDTs), maximizing $N_s/\sqrt{N_s + N_b}$, where N_s and N_b are signal and background yields in simulation.

To reconstruct the prompt photon, we select a cluster of ECL hits with no associated track. We require that the photon's energy in the center-of-mass (c.m.) frame is the highest in the event and exceeds 1.6 GeV. The dominant background is from photons arising from π^0 and η decays; these are rejected with a BDT-based algorithm [43]. We apply a selection on the BDT output that, according to simulation, rejects 83% (45%) of photons from π^0 (η) decays while retaining 92% (99%) of prompt signal photons.

We reconstruct $K_S^0 \to \pi^+\pi^-$ candidates using two oppositely charged tracks. The K_S^0 candidates are selected with an invariant mass in the range $|m(\pi^+\pi^-) - m_{K_S^0}| < 34$ MeV/c^2, where $m_{K_S^0}$ is the known K_S^0 mass [44]. This range corresponds to $\pm 2.6\sigma$ in resolution. To further reduce background, we employ another BDT to form two classifiers: K_S^0 likeness and Λ likeness, which are based on kinematic and PID information. We apply selection criteria on these classifiers that retain 97% of signal K_S^0 decays, according to simulation, while rejecting 67% of candidates due to Λ's and 98% of other background candidates.

We reconstruct $\pi^0 \to \gamma\gamma$ candidates using pairs of ECL clusters with no associated tracks. We require a cluster energy greater than 22.5 (20.0) MeV in the forward end cap (barrel and backward end cap). Photon pairs having an invariant mass $m(\gamma\gamma) \in (104, 164)$ MeV/c^2, corresponding to 2σ in resolution, are selected as π^0 candidates. We also require that the π^0 momentum exceeds 430 MeV/c. This requirement retains 92% of signal π^0's, according to simulation, while rejecting 74% of background π^0's.

We reconstruct $B_{\rm sig}$ candidates by combining γ, K_S^0, and π^0 candidates. We select $B_{\rm sig}$ candidates using the beam-energy-constrained mass $M_{\rm bc} \equiv \sqrt{E_{\rm beam}^{*2}/c^4 - \mathbf{p}_B^{*2}/c^2}$, and energy difference $\Delta E \equiv E_B^* - E_{\rm beam}^*$, where $E_{\rm beam}^*$ is the beam energy and E_B^* and $\mathbf{p}_B^*$ are the reconstructed energy and momentum of the $B_{\rm sig}$ candidate. All quantities are evaluated in the c.m. frame. We retain $B_{\rm sig}$ candidates satisfying $5.20 < M_{\rm bc} < 5.29$ GeV/c^2 and $-0.5 < \Delta E < 0.5$ GeV. Almost half (45%) of events have multiple $B_{\rm sig}$ candidates, with 96% of these due to multiple π^0 candidates. To identify the correct $B_{\rm sig}$ candidate, we use a BDT-based classifier based on the properties of the π^0 candidate [45]. We retain the $B_{\rm sig}$ candidate with the highest π^0 BDT classifier value. If multiple candidates share the same π^0, we choose the candidate with the highest value of K_S^0 likeness. These criteria select the correct $B_{\rm sig}$ candidate in 85% of simulated events with multiple candidates. The invariant mass of the $K_S^0\pi^0$ system, $m(K_S^0\pi^0)$, is required to be in the range 0.6–1.8 GeV/c^2. We define mass region 1 (MR1) as $m(K_S^0\pi^0) \in (0.8, 1.0)$ GeV/c^2, which is dominated by the $K^*(892)^0$ meson, and mass region 2 (MR2) as $m(K_S^0\pi^0) \in (0.6, 0.8) \cup (1.0, 1.8)$ GeV/c^2.

We measure the decay vertex positions of $B_{\rm sig}$ and $B_{\rm tag}$ in kinematic fits. The $B_{\rm sig}$ vertex is determined by a fit to the entire decay chain [53]. This fit includes the constraint that the $B_{\rm sig}$ trajectory be consistent with originating from the e^+e^- interaction point (IP). The IP is measured regularly by averaging over $e^+e^- \to \mu^+\mu^-$ events. For the $B_{\rm tag}$ vertex [54], the tracks used must have a distance of closest approach to the IP within 0.5 cm in the r–ϕ plane and within 2.0 cm along the z axis. We also require that each track have at least one hit in each of the PXD, SVD, and CDC subdetectors, and a momentum greater than 50 MeV/c.

We calculate the decay time Δt as $(\ell_{\rm sig} - \ell_{\rm tag})/\beta\gamma c$, where $\ell_{\rm sig}$ ($\ell_{\rm tag}$) is the $B_{\rm sig}$ ($B_{\rm tag}$) decay vertex position projected along the $\Upsilon(4S)$ boost direction, and $\beta\gamma$ is the

Lorentz boost factor of the $\Upsilon(4S)$ in the lab frame. This calculation applies to events satisfying the following "TD" (time-dependent) criteria. For the $B_{\rm sig}$ vertex, both pions from the K^0_S must have at least one SVD hit; the χ^2 of the vertex fit must be less than 30 (100) for tracks (overall); and the uncertainty on $\ell_{\rm sig}$, $\sigma_{\ell_{\rm sig}}$, must be less than 500 μm. For the $B_{\rm tag}$ vertex, the reduced χ^2 of the vertex fit must be less than 100, and $\sigma_{\ell_{\rm tag}}$ must be less than 500 μm. Events that do not satisfy these criteria are classified as "TI" (time-integrated); they are included in the fit (described below) to improve the precision on C.

The flavor q of $B_{\rm tag}$ is determined using a combination of BDT algorithms [55]. The combination outputs the product qr, where r is a quality factor that ranges from zero for no flavor information to 1.0 for unambiguous flavor assignment. As the tagging efficiency and signal purity depend on r, we divide the data into seven r bins, each containing a similar number of events. For each r bin, the wrong-tag fraction w and the difference Δw between B^0 and $\bar{B}^0$ tags are determined using flavor-specific B decays [56]. The effective tagging efficiency, $\varepsilon_{\rm eff} = \Sigma_i \varepsilon^i_{\rm tag}(1-2w_i)^2$, is $(31.69 \pm 0.35)\%$, where $\varepsilon^i_{\rm tag}$ is the probability for a $B^0 \to K^0_S\pi^0\gamma$ decay to be flavor-tagged with r in the ith bin.

We train two BDT classifiers to discriminate signal from $q\bar{q}$ background, separately for MR1 and MR2 candidates. The classifiers use event topology variables [45], and the classifier thresholds are optimized separately for each r bin. According to simulation, these thresholds retain 77% (74%) of signal decays while rejecting 95% (89%) of $q\bar{q}$ background for MR1 (MR2).

As a control mode, we reconstruct the decay $B^+ \to K^0_S\pi^+\gamma$, which does not exhibit mixing-induced CP violation. This decay, when the primary π^+ track is ignored, has the same vertex resolution as the signal $B^0 \to K^0_S\pi^0\gamma$ decay, as the contribution of the π^0 candidate to the signal vertex resolution is negligible.

The signal and background yields are determined from an unbinned maximum-likelihood fit to the $M_{\rm bc}$–ΔE distribution. We fit events in the ranges $5.23 < M_{\rm bc} < 5.29$ GeV/c^2 and $-0.4 < \Delta E < 0.3$ GeV. We combine the TD and TI samples, as they (both for data and for simulated signal and background events) show negligible differences in these variables. We model the $M_{\rm bc}$–ΔE probability density functions (PDFs) for signal and $B\bar{B}$ background using simulation. Kernel density estimation [57] is used to account for $M_{\rm bc}$–ΔE correlations. The $q\bar{q}$ background is modeled with the product of an ARGUS function [58] for $M_{\rm bc}$ and a second-order polynomial for ΔE. The signal and $B\bar{B}$ yields, and the $q\bar{q}$ shape parameters, are floated in the fit, while the total yield is fixed. To calculate signal yields, we define a signal-enhanced region $5.27 < M_{\rm bc} < 5.29$ GeV/c^2 and $-0.2 < \Delta E < 0.1$ GeV. For $B^0 \to K^*(892)^0\gamma$ events, the efficiency in this region is $(22.8 \pm 0.1)\%$ for MR1. The fitted $M_{\rm bc}$ and ΔE distributions and projections of the fit result are shown in Fig. 1. The resulting signal and $B\bar{B}$ yields are listed in Table I.

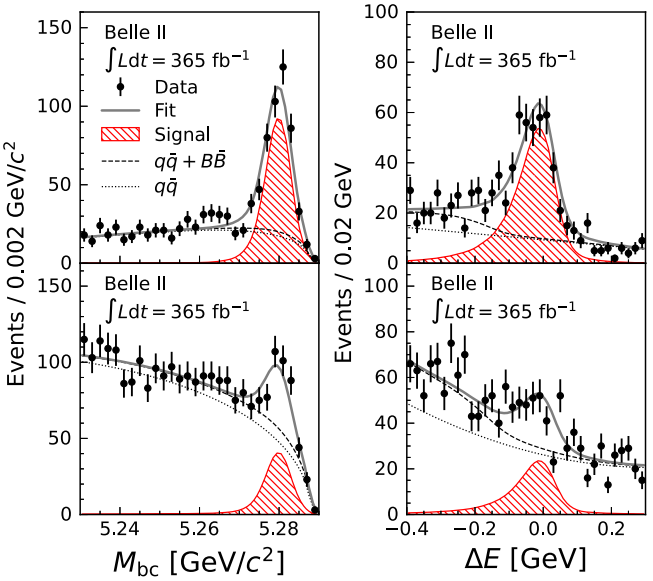

FIG. 1. Distributions of $M_{\rm bc}$ (left) and ΔE (right) for MR1 (top) and MR2 (bottom), with fit results overlaid. The $M_{\rm bc}$ (ΔE) distribution corresponds to the ΔE ($M_{\rm bc}$) signal-enhanced region.

The Δt PDF consists of signal and background components weighted by their fractions as determined from the $M_{\rm bc}$–ΔE fit. For the TD category, the PDF is described as

$$P_{\rm TD}(\Delta t, q) = \int_{-\infty}^{\infty} [f_{\rm sig}\mathcal{P}_{\rm sig}(\Delta t', q)R_{\rm sig}(\Delta t - \Delta t') + (1-f_{\rm sig})f_{B\bar{B}}\mathcal{P}_{B\bar{B}}(\Delta t', q)R_{B\bar{B}}(\Delta t - \Delta t')]d\Delta t' + (1-f_{\rm sig})(1-f_{B\bar{B}})\mathcal{P}_{q\bar{q}}(\Delta t), \quad (2)$$

$$\mathcal{P}_{\rm sig}(\Delta t', q) = \frac{1}{4\tau_{B^0}} e^{-\frac{|\Delta t'|}{\tau_{B^0}}} \Big\{ 1 - q\Delta w + q(1-2w) \times [S\sin(\Delta m_d \Delta t') - C\cos(\Delta m_d \Delta t')] \Big\}, \quad (3)$$

TABLE I. Signal and control sample yields in the signal-enhanced region. Also listed is the signal-to-background ratio (N_s/N_b), where N_b includes all backgrounds.

Sample	Signal yield	$B\bar{B}$ background yield	N_s/N_b
$B^0 \to K^0_S\pi^0\gamma$ in MR1	385 ± 24	20 ± 8	2.36
$B^0 \to K^0_S\pi^0\gamma$ in MR2	171 ± 23	69 ± 19	0.34
$B^+ \to K^0_S\pi^+\gamma$	843 ± 34	55 ± 10	2.68

$$\mathcal{P}_{B\bar{B}}(\Delta t', q) = \frac{1}{4\tau_{B\bar{B}}} e^{-\frac{|\Delta t'|}{\tau_{B\bar{B}}}}(1 - q\Delta w), \tag{4}$$

where $f_{\rm sig}$ is the event-by-event signal probability, $f_{B\bar{B}}$ is the $B\bar{B}$ background probability relative to that of all background components, $\mathcal{P}_{\rm sig}(\Delta t', q)$ and $\mathcal{P}_{B\bar{B}}(\Delta t', q)$ are the signal and $B\bar{B}$ background PDFs taking into account the effect of w and Δw, $\mathcal{P}_{q\bar{q}}(\Delta t)$ is the $q\bar{q}$ PDF, and $R_{\rm sig}$ and $R_{B\bar{B}}$ are the proper-time resolution functions for signal and $B\bar{B}$ background [45]. We fix τ_{B^0} and Δm_d to their known values [44] and the effective lifetime of the $B\bar{B}$ background, $\tau_{B\bar{B}}$, to the value determined from simulation. The fractions $f_{\rm sig}$ and $f_{B\bar{B}}$ are taken from the previous fit. The only floated parameters are S and C.

The resolution functions, $R_{\rm sig}$ and $R_{B\bar{B}}$, are described by convolving three components: detector resolution for $B_{\rm sig}$ and $B_{\rm tag}$ decay vertices, bias due to the secondary decay vertex of intermediate charm states in $B_{\rm tag}$ decays, and a correction to the boost factors due to the small momenta of the B mesons in the c.m. frame. The last component depends on $\cos\theta_B^*$, where θ_B^* is the angle in the c.m. frame between the B^0 momentum and the $\Upsilon(4S)$ boost direction [59]. We model the detector resolution for $B_{\rm sig}$ ($B_{\rm tag}$) vertex on an event-by-event basis, including the dependence on $\sigma_{\ell_{\rm sig}}$ ($\sigma_{\ell_{\rm tag}}$) and the χ^2 from the vertex fit. The resolution function parameters are determined from simulated samples generated with five parameters of a helixlike trajectory [60] calibrated from data. The data used consist of cosmic ray events in which a cosmic ray track traversing the PXD or SVD is reconstructed as two outgoing tracks from the IP.

For $B\bar{B}$ background, the $B_{\rm sig}$ vertex resolution is the same as that of the signal component due to the high purity of K_S^0 candidates, while the $B_{\rm tag}$ vertex suffers from contamination by tracks coming from the background $B_{\rm sig}$ decay. We adjust $\tau_{B\bar{B}}$ in $\mathcal{P}_{B\bar{B}}$ and parameters of the $B\bar{B}$ resolution function to account for the smeared vertex position and the typically shorter decay-time difference. We model $\mathcal{P}_{q\bar{q}}(\Delta t)$ using three Gaussian functions, whose shape parameters are determined from a fit to an $M_{\rm bc}$–ΔE sideband in data defined as $5.23 < M_{\rm bc} < 5.255$ GeV/c^2, $-0.5 < \Delta E < 0.3$ GeV, and $(M_{\rm bc} - 5.23\ {\rm GeV}/c^2) < (\Delta E + 0.45\ {\rm GeV})/14c^2$.

The PDF $P_{\rm TD}$ depends on $\cos\theta_B^*$, $\sigma_{\ell_{\rm sig}}$, $\sigma_{\ell_{\rm tag}}$, the vertex-fit χ^2's, and r (through Δw) [45]. If signal and background events are distributed differently in these variables, then including them in the PDF can introduce bias [61]. Among these variables, only r and $\cos\theta_B^*$ differ noticeably between signal and backgrounds, and to alleviate bias we include additional PDFs for them in the likelihood function [61]. The r and $\cos\theta_B^*$ distributions for signal and $B\bar{B}$ background are determined from simulation, while those for $q\bar{q}$ background are taken from the $M_{\rm bc}$–ΔE sideband in data.

For the TI category, the PDF is expressed as

$$\begin{aligned} P_{\rm TI}(q) = {} & f_{\rm sig}\left(\frac{1}{2}\right)\left[1 - q\Delta w - q(1-2w)\frac{C}{1+\Delta m_d^2\tau_{B^0}^2}\right] \\ & + (1 - f_{\rm sig}) f_{B\bar{B}}\left(\frac{1 - q\Delta w}{2}\right) \\ & + (1 - f_{\rm sig})(1 - f_{B\bar{B}})\left(\frac{1}{2}\right), \end{aligned} \tag{5}$$

where only the C parameter is extracted in the fit.

We simultaneously fit the TD and TI samples in the signal-enhanced region, floating the common C parameter. The results are $S = 0.00^{+0.27}_{-0.26}$ and $C = 0.10 \pm 0.13$ for MR1 events, and $S = 0.04^{+0.45}_{-0.44}$ and $C = -0.06 \pm 0.25$ for MR2 events. The statistical correlation between S and C is -0.005 in MR1 and $+0.011$ in MR2. Figure 2 shows the Δt distribution along with the fit result. No significant time-dependent asymmetries are observed.

We perform various cross-checks to confirm the validity of our fit procedure. We fit for the B^0 lifetime in the MR1 and MR2 samples and obtain 1.55 ± 0.14 ps and 1.58 ± 0.24 ps, respectively, which are consistent with the world average [44]. We also perform studies of the control mode $B^+ \to K_S^0\pi^+\gamma$. The lifetime fit obtains 1.68 ± 0.09 ps, which is consistent with the B^+ lifetime. The difference between B^+ vertices with and without the π^+ track is consistent with the $B_{\rm sig}$ vertex resolution function. We fit for CP violation and obtain $S = 0.05 \pm 0.09$ and $C = 0.03 \pm 0.05$, which are consistent with $S = 0$ and the world average $C = 0.014 \pm 0.018$ [44].

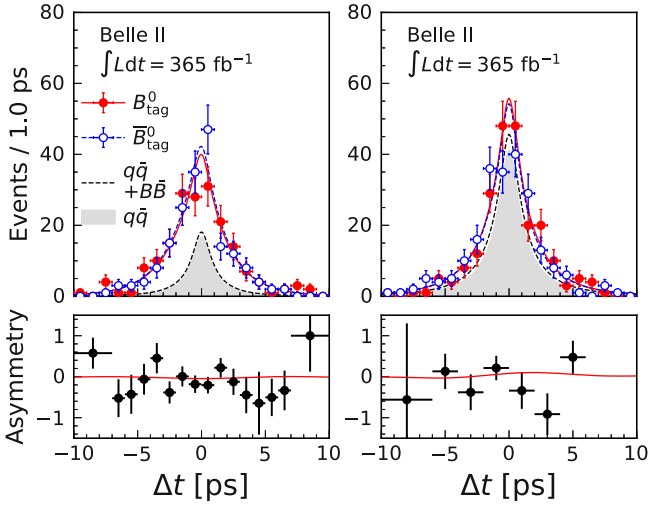

FIG. 2. Δt distributions for MR1 (left) and MR2 (right) with the fit result superimposed. The asymmetry $[N_s(B^0_{\rm tag}) - N_s(\bar{B}^0_{\rm tag})]/[N_s(B^0_{\rm tag}) + N_s(\bar{B}^0_{\rm tag})]$ is calculated in each Δt bin using ${}_s\mathcal{P}lot$ [62] and plotted in the bottom panels along with the fit result.

We consider various sources of systematic uncertainty. We repeat the analysis with shifted scaling factors for the track momentum and cluster energy and take the deviation from the nominal results as the uncertainty. In a similar manner, we treat four sources of uncertainties for the vertex measurements: possible detector misalignments, imperfect understanding of the IP profile measurement [56], corrections to uncertainties on the track helix parameters, and the TD criteria. We assess the effect of uncertainties in w and Δw by varying them by their uncertainties and refitting the data. We also simulate the effect of a difference in $\epsilon^i_{\rm tag}$ between $B^0_{\rm tag}$ and $\bar{B}^0_{\rm tag}$ decays. The uncertainties due to fixed parameters for $M_{\rm bc}$, ΔE, and $\cos\theta^*_B$ PDFs and r-bin fractions in signal modeling, including $f_{\rm sig}$ and $f_{B\bar{B}}$, are also evaluated by refitting. We simulate potential mismodeling of $M_{\rm bc}$–ΔE distributions and potential bias from the modeling of $\sigma_{\ell_{\rm sig}}$, $\sigma_{\ell_{\rm tag}}$ and the vertex fit χ^2's [61]. The uncertainties due to limited statistics of the dataset used for kernel density estimation are evaluated with the bootstrap method [63].

We consider uncertainties from the modeling and parameters of the Δt resolution function by varying these parameters by their uncertainties and refitting. The differences between these results and our nominal result are taken as uncertainties. We evaluate the uncertainties arising from τ_{B^0} and Δm_d in a similar manner [44].

We study the impact of an asymmetry in $B\bar{B}$ backgrounds. We generate samples with asymmetric backgrounds and refit using our nominal (symmetric) $B\bar{B}$ background PDF. The change in the fit results is assigned as an uncertainty. The asymmetries simulated correspond to the world average values of S, C for $b \to sq\bar{q}$ decays, and to maximum values of S, C (± 1) for $b \to s\gamma$ decays.

We evaluate the bias from tag-side interference [64] assuming $S = C = 0$. The dominant uncertainties come from the scaling factors for cluster energy, the vertex quality selection criteria, the $B\bar{B}$ background asymmetry, and the tag-side interference. The total systematic uncertainties, listed in Table II, are calculated as the sum in quadrature of all individual systematic uncertainties.

TABLE II. Summary of systematic uncertainties.

	$K^{*0}\gamma$		$K^0_S\pi^0\gamma$	
Source	S	C	S	C
E and p scales	± 0.017	± 0.015	± 0.083	± 0.047
Vertex measurement	± 0.021	± 0.009	± 0.023	± 0.036
Flavor tagging	± 0.005	$^{+0.012}_{-0.009}$	$^{+0.008}_{-0.009}$	$^{+0.013}_{-0.009}$
Signal modeling	± 0.003	± 0.003	± 0.032	± 0.013
Δt resolution function	± 0.014	± 0.009	± 0.031	± 0.013
τ_{B^0} and Δm_d	< 0.001	< 0.001	± 0.003	< 0.001
$B\bar{B}$ background asymmetry	$^{+0.007}_{-0.008}$	± 0.011	$^{+0.030}_{-0.026}$	$^{+0.049}_{-0.051}$
Tag-side interference	± 0.003	± 0.028	± 0.003	± 0.028
Total	± 0.032	$^{+0.037}_{-0.038}$	$^{+0.102}_{-0.101}$	± 0.085

In summary, we measure the time-dependent CP asymmetry in $B^0 \to K^0_S\pi^0\gamma$ decays using $(388 \pm 6) \times 10^6$ $B\bar{B}$ events collected by the Belle II detector. These decays are sensitive to right-handed currents arising from BSM physics. We perform these measurements for two $m(K^0_S\pi^0)$ mass regions corresponding to $K^{*0} \to K^0_S\pi^0$ and nonresonant decays. We obtain CP-violating parameters

$$S = 0.00^{+0.27}_{-0.26} \pm 0.03, \qquad C = 0.10 \pm 0.13 \pm 0.04 \tag{6}$$

for the K^{*0} resonant region and

$$S = 0.04^{+0.45}_{-0.44} \pm 0.10, \qquad C = -0.06 \pm 0.25 \pm 0.09 \tag{7}$$

for the nonresonant region, where the uncertainties are statistical and systematic, respectively. The measured S values agree with SM predictions [18,19] within 1 standard deviation. Our results have improved precision with respect to previous measurements [22,23]. The improvements mostly result from a refined K^0_S identification algorithm and a large-acceptance silicon vertex detector [33]. The improved precision should further constrain the BSM parameter space [4–11].

Acknowledgments—This work, based on data collected using the Belle II detector, which was built and commissioned prior to March 2019, was supported by Higher Education and Science Committee of the Republic of Armenia Grant No. 23LCG-1C011; Australian Research Council and Research Grants No. DP200101792, No. DP210101900, No. DP210102831, No. DE220100462, No. LE210100098, and No. LE230100085; Austrian Federal Ministry of Education, Science and Research, Austrian Science Fund No. P 34529, No. J 4731, No. J 4625, and No. M 3153, and Horizon 2020 ERC Starting Grant No. 947006 "InterLeptons"; Natural Sciences and Engineering Research Council of Canada, Compute Canada and CANARIE; National Key R&D Program of China under Contract No. 2022YFA1601903, National Natural Science Foundation of China and Research Grants No. 11575017, No. 11761141009, No. 11705209, No. 11975076, No. 12135005, No. 12150004, No. 12161141008, and No. 12175041, and Shandong Provincial Natural Science Foundation Project No. ZR2022JQ02; the Czech Science Foundation Grant No. 22-18469S and Charles University Grant Agency project No. 246122; European Research Council, Seventh Framework PIEF-GA-2013-622527, Horizon 2020 ERC-Advanced Grants No. 267104 and No. 884719, Horizon 2020 ERC-Consolidator Grant No. 819127, Horizon 2020 Marie Sklodowska-Curie Grant Agreement No. 700525 "NIOBE" and

No. 101026516, and Horizon 2020 Marie Sklodowska-Curie RISE project JENNIFER2 Grant Agreement No. 822070 (European grants); L'Institut National de Physique Nucléaire et de Physique des Particules (IN2P3) du CNRS and L'Agence Nationale de la Recherche (ANR) under Grant No. ANR-21-CE31-0009 (France); BMBF, DFG, HGF, MPG, and AvH Foundation (Germany); Department of Atomic Energy under Project Identification No. RTI 4002, Department of Science and Technology, and UPES SEED funding programs No. UPES/R&D-SEED-INFRA/17052023/01 and No.~UPES/R&D-SOE/20062022/06 (India); Israel Science Foundation Grant No. 2476/17, U.S.-Israel Binational Science Foundation Grant No. 2016113, and Israel Ministry of Science Grant No. 3-16543; Istituto Nazionale di Fisica Nucleare and the Research Grants BELLE2; Japan Society for the Promotion of Science, Grant-in-Aid for Scientific Research Grants No. 16H03968, No. 16H03993, No. 16H06492, No. 16K05323, No. 17H01133, No. 17H05405, No. 18K03621, No. 18H03710, No. 18H05226, No. 19H00682, No. 20H05850, No. 20H05858, No. 22H00144, No. 22K14056, No. 22K21347, No. 23H05433, No. 26220706, and No. 26400255, and the Ministry of Education, Culture, Sports, Science, and Technology (MEXT) of Japan; National Research Foundation (NRF) of Korea Grants No. 2016R1-D1A1B-02012900, No. 2018R1-A6A1A-06024970, No. 2021R1-A6A1A-03043957, No. 2021R1-F1A-1060423, No. 2021R1-F1A-1064008, No. 2022R1-A2C-1003993, No. 2022R1-A2C-1092335, No. RS-2023-00208693, No. RS-2024-00354342 and No. RS-2022-00197659, Radiation Science Research Institute, Foreign Large-Size Research Facility Application Supporting project, the Global Science Experimental Data Hub Center, the Korea Institute of Science and Technology Information (K24L2M1C4) and KREONET/GLORIAD; Universiti Malaya RU grant, Akademi Sains Malaysia, and Ministry of Education Malaysia; Frontiers of Science Program Contracts No. FOINS-296, No. CB-221329, No. CB-236394, No. CB-254409, and No. CB-180023, and SEP-CINVESTAV Research Grant No. 237 (Mexico); the Polish Ministry of Science and Higher Education and the National Science Center; the Ministry of Science and Higher Education of the Russian Federation and the HSE University Basic Research Program, Moscow; University of Tabuk Research Grants No. S-0256-1438 and No. S-0280-1439 (Saudi Arabia); Slovenian Research Agency and Research Grants No. J1-9124 and No. P1-0135; Agencia Estatal de Investigacion, Spain Grant No. RYC2020-029875-I and Generalitat Valenciana, Spain Grant No. CIDEGENT/2018/020; The Knut and Alice Wallenberg Foundation (Sweden), Contracts No. 2021.0174 and No. 2021.0299; National Science and Technology Council, and Ministry of Education (Taiwan); Thailand Center of Excellence in Physics; TUBITAK ULAKBIM (Turkey); National Research Foundation of Ukraine, Project No. 2020.02/0257, and Ministry of Education and Science of Ukraine; the U.S. National Science Foundation and Research Grants No. PHY-1913789 and No. PHY-2111604, and the U.S. Department of Energy and Research Awards No. DE-AC06-76RLO1830, No. DE-SC0007983, No. DE-SC0009824, No. DE-SC0009973, No. DE-SC0010007, No. DE-SC0010073, No. DE-SC0010118, No. DE-SC0010504, No. DE-SC0011784, No. DE-SC0012704, No. DE-SC0019230, No. DE-SC0021274, No. DE-SC0021616, No. DE-SC0022350, No. DE-SC0023470; and the Vietnam Academy of Science and Technology (VAST) under Grants No. NVCC.05.12/22-23 and No. DL0000.02/24-25. These acknowledgements are not to be interpreted as an endorsement of any statement made by any of our institutes, funding agencies, governments, or their representatives. We thank the SuperKEKB team for delivering high-luminosity collisions; the KEK cryogenics group for the efficient operation of the detector solenoid magnet and IBBelle on site; the KEK Computer Research Center for on-site computing support; the NII for SINET6 network support; and the raw-data centers hosted by BNL, DESY, GridKa, IN2P3, INFN, and the University of Victoria.

[1] S. Bertolini, F. Borzumati, A. Masiero, and G. Ridolfi, Nucl. Phys. **B353**, 591 (1991).
[2] P. L. Cho and M. Misiak, Phys. Rev. D **49**, 5894 (1994).
[3] K. Fujikawa and A. Yamada, Phys. Rev. D **49**, 5890 (1994).
[4] D. Atwood, M. Gronau, and A. Soni, Phys. Rev. Lett. **79**, 185 (1997).
[5] D. Atwood, T. Gershon, M. Hazumi, and A. Soni, Phys. Rev. D **71**, 076003 (2005).
[6] M. Blanke, B. Shakya, P. Tanedo, and Y. Tsai, J. High Energy Phys. 08 (2012) 038.
[7] D. Becirevic, E. Kou, A. Le Yaouanc, and A. Tayduganov, J. High Energy Phys. 08 (2012) 090.
[8] Y. Shimizu, M. Tanimoto, and K. Yamamoto, Phys. Rev. D **87**, 056004 (2013).
[9] E. Kou, C.-D. Lü, and F.-S. Yu, J. High Energy Phys. 12 (2013) 102.
[10] R. Malm, M. Neubert, and C. Schmell, J. High Energy Phys. 04 (2016) 042.
[11] H. Eberl, K. Hidaka, E. Ginina, and A. Ishikawa, Phys. Rev. D **104**, 075025 (2021).
[12] A. B. Carter and A. I. Sanda, Phys. Rev. Lett. **45**, 952 (1980).
[13] A. B. Carter and A. I. Sanda, Phys. Rev. D **23**, 1567 (1981).
[14] I. I. Y. Bigi and A. I. Sanda, Nucl. Phys. **B193**, 85 (1981).
[15] Here, we neglect CP violation in B^0–$\bar{B}^0$ mixing.
[16] The coefficients $(S, -C)$ are written (S, A) elsewhere.
[17] Charge-conjugate modes are included unless explicitly stated otherwise.
[18] M. Matsumori and A. I. Sanda, Phys. Rev. D **73**, 114022 (2006).

[19] P. Ball, G. W. Jones, and R. Zwicky, Phys. Rev. D **75**, 054004 (2007).
[20] B. Grinstein, Y. Grossman, Z. Ligeti, and D. Pirjol, Phys. Rev. D **71**, 011504(R) (2005).
[21] B. Grinstein and D. Pirjol, Phys. Rev. D **73**, 014013 (2006).
[22] Y. Ushiroda *et al.* (Belle Collaboration), Phys. Rev. D **74**, 111104 (2006).
[23] B. Aubert *et al.* (BABAR Collaboration), Phys. Rev. D **78**, 071102 (2008).
[24] R. Aaij *et al.* (LHCb Collaboration), Phys. Rev. Lett. **123**, 081802 (2019).
[25] R. Aaij *et al.* (LHCb Collaboration), J. High Energy Phys. 12 (2020) 081.
[26] R. Aaij *et al.* (LHCb Collaboration), Phys. Rev. D **105**, L051104 (2022).
[27] T. Horiguchi *et al.* (Belle Collaboration), Phys. Rev. Lett. **119**, 191802 (2017).
[28] B. Aubert *et al.* (BABAR Collaboration), Phys. Rev. Lett. **103**, 211802 (2009).
[29] R. Aaij *et al.* (LHCb Collaboration), Nucl. Phys. **B867**, 1 (2013).
[30] I. Adachi *et al.* (Belle II Collaboration), arXiv:2407.00965.
[31] T. Abe *et al.* (Belle II Collaboration), arXiv:1011.0352.
[32] K. Akai, K. Furukawa, and H. Koiso (SuperKEKB Group), Nucl. Instrum. Methods Phys. Res., Sect. A **907**, 188 (2018).
[33] K. Adamczyk *et al.* (Belle II SVD Collaboration), J. Instrum. **17**, P11042 (2022).
[34] D. Kotchetkov *et al.*, Nucl. Instrum. Methods Phys. Res., Sect. A **941**, 162342 (2019).
[35] A. L. Kagan and M. Neubert, Eur. Phys. J. C **7**, 5 (1999).
[36] D. J. Lange, Nucl. Instrum. Methods Phys. Res., Sect. A **462**, 152 (2001).
[37] S. Jadach, B. F. L. Ward, and Z. Wąs, Comput. Phys. Commun. **130**, 260 (2000).
[38] T. Sjöstrand, S. Ask, J. R. Christiansen, R. Corke, N. Desai, P. Ilten, S. Mrenna, S. Prestel, C. O. Rasmussen, and P. Z. Skands, Comput. Phys. Commun. **191**, 159 (2015).
[39] S. Jadach, J. H. Kuhn, and Z. Wąs, Comput. Phys. Commun. **64**, 275 (1990).
[40] S. Agostinelli *et al.* (GEANT4 Collaboration), Nucl. Instrum. Methods Phys. Res., Sect. A **506**, 250 (2003).
[41] T. Kuhr *et al.* (Belle II Framework Software Group), Comput. Software Big Sci. **3**, 1 (2019).
[42] R. Storn and K. Price, J. Global Optim. **11**, 341 (1997).
[43] I. Adachi *et al.* (Belle II Collaboration), arXiv:2407.08984.
[44] R. L. Workman *et al.* (Particle Data Group), Prog. Theor. Exp. Phys. **2022**, 083C01 (2022).
[45] See Supplemental Material at http://link.aps.org/supplemental/10.1103/PhysRevLett.134.011802 for additional information about the BDT-based classifier, which includes Ref. [46], for additional information about the BDT classifiers, which includes Refs. [47–52], and for additional information about the proper-time resolution functions.
[46] A. Khotanzad and Y. Hong, IEEE Trans. Pattern Anal. Mach. Intell. **12**, 489 (1990).
[47] G. C. Fox and S. Wolfram, Phys. Rev. Lett. **41**, 1581 (1978).
[48] Ed. A. J. Bevan, B. Golob, Th. Mannel, S. Prell, and B. D. Yabsley, Eur. Phys. J. C **74**, 3026 (2014).
[49] S. Brandt *et al.*, Phys. Lett. **12**, 57 (1964).
[50] E. Farhi, Phys. Rev. Lett. **39**, 1587 (1977).
[51] S. H. Lee *et al.* (Belle Collaboration), Phys. Rev. Lett. **91**, 261801 (2003).
[52] D. M. Asner *et al.* (CLEO Collaboration), Phys. Rev. D **53**, 1039 (1996).
[53] J. F. Krohn *et al.* (Belle II Analysis Software Group), Nucl. Instrum. Methods Phys. Res., Sect. A **976**, 164269 (2020).
[54] S. Dey and A. Soffer, Springer Proc. Phys. **248**, 411 (2020).
[55] F. Abudinén *et al.* (Belle II Collaboration), Eur. Phys. J. C **82**, 283 (2022).
[56] I. Adachi *et al.* (Belle II Collaboration), Phys. Rev. D **107**, L091102 (2023), the calibration described in this note has been updated with the larger 365 fb^{-1} dataset used in this analysis.
[57] K. S. Cranmer, Comput. Phys. Commun. **136**, 198 (2001).
[58] H. Albrecht *et al.* (ARGUS Collaboration), Phys. Lett. B **241**, 278 (1990).
[59] H. Tajima *et al.*, Nucl. Instrum. Methods Phys. Res., Sect. A **533**, 370 (2004).
[60] V. Bertacchi *et al.* (Belle II Tracking Group), Comput. Phys. Commun. **259**, 107610 (2021).
[61] G. Punzi, eConf **C030908**, WELT002 (2003), https://www.slac.stanford.edu/econf/C030908/proceedings.html.
[62] M. Pivk and F. R. Le Diberder, Nucl. Instrum. Methods Phys. Res., Sect. A **555**, 356 (2005).
[63] B. Efron, Ann. Stat. **7**, 1 (1979).
[64] O. Long, M. Baak, R. N. Cahn, and D. P. Kirkby, Phys. Rev. D **68**, 034010 (2003), we take $r' = 0.015$ and $\delta = \pm\pi/2$ to evaluate this systematic effect.